Forward analysis of Love wave scattering due to a cavity-like defect

Chen Yang[a], Bin Wang[a], Zhenghua Qian[a*]

[a]*State Key Laboratory of Mechanics and Control of Mechanical Structures, Nanjing University of Aeronautics and Astronautics, 29 Yudao Jie, Nanjing 210016, China*

[*]*Correspondence should be addressed to Zhenghua Qian; qianzh@nuaa.edu.cn*

Abstract

This paper presents a modified boundary element method (BEM) to solve the scattering problem of Love surface wave from a two-dimensional cavity defect. Because of the truncation of BEM models at a far distance from the cavity, spurious reflected waves are generated. In order to eliminate the unwanted reflections, the guided Love-wave displacement patterns are assumed on the far-field infinite boundaries previously omitted by model truncation, and they are incorporated into the BEM equation set as modified items. The numerical results are verified by theoretical solutions of far-field Green's functions. Additional parametric studies are performed to find out the influence of truncation distance and defects' geometric characters on the accuracy of scattered wave solutions.

Keywords: Love wave; scattering; boundary element method.

1. Introduction

The ultrasonic nondestructive testing (NDT) techniques have wide applications for quantitative characterizations of mechanical properties and detection and characterization of cracks and defects. Traditional ultrasonic testing techniques using bulk waves are very time-consuming, since these techniques need an overall inspection of the structure. However, ultrasonic guided waves are attractive for inspection of long-range or wide area structures because they can travel considerable distances and therefore scan large regions for defects in shorter testing time [1,2].

The current NDT applications of guided waves include pitch-catch [3] or pulse-echo [4] flaw detection method, phased array configuration [5] diffraction tomography [6] and so on. Generally, these methods make use of time-of-flight (TOF) of the reflected waves from inner defects to locate their approximate positions.

However, further information (e.g. defect shapes or depths) cannot be further utilized because of the complexity of guided waves. Hence, the quantitative non-destructive testing requires a thorough understanding of surface wave scattering in forward and inverse aspects. For the forward problem, we need to solve the near- and far-fields accurately and obtain the scattering coefficients for following inverse reconstruction [7~9].

The Love wave is a special kind of guided waves that travels along the surface of elastic layer covered on top of an elastic half-plane. The scattered Love waves are relied on to investigate underground information in geotechnique engineering, earthquake engineering [10], or detecting flaws and cracks at the bounding interface in non-destructive testing applications [11]. An effective utilization of the Love wave requires a thorough understanding of its scattering phenomenon.

For the calculation of scattered wave field over a finite domain, various technologies can be implied, such as Finite element method (FEM) [12], BEM [13], Mode-exciting method [14], Matrix theory [15], and so on. However, for the forward analysis of a half-plane, the BEM is especially effective, since only the interfaces and flaw boundaries need to be meshed. There are BEM approaches using two kinds of Green's functions: half-space and full-space. Using the former one, only the flawed portion needs to be meshed, however, the Green's function cannot be written in a closed form. Conversely, using the latter one, the whole interface should be meshed, however, the Green's function is much simpler. Thus, for the forward analysis of Love-wave, we adopt the latter one.

However, in traditional BEM approaches, due to the inevitable artificial truncation of BEM model, spurious reflected waves are introduced in the final results of scattered wave field, which causes considerable error. Another big challenge to solute the scattering problem is the existence of multiple dispersive modes of Love waves at a certain frequency along with the modal conversion, due to the interaction at the damage location.

Here, a modified BEM for calculating scattered Love waves is introduced. In this paper, the guided Love-wave displacement patterns are assumed on the far-field infinite boundaries previously omitted, and they

are incorporated into BEM equation sets as the modified items. With this improvement, the spurious reflected waves are eliminated. The numerical results are verified by theoretical far-field Green's functions [16,17]. Furthermore, various parametric studies of the influence of defect locations, geometrical shapes and size, on the calculations of Love-wave scattered fields are carried out in the later sections, which have potential values for investigating forward problem, or inverse problem of flaw reconstruction based on surface waves.

2. Statement of the problem

The Love surface wave propagates along the surface of elastic layer of thickness H covered on top of a homogeneous, elastic half-plane, containing a cavity of arbitrary shape on the bonding interface of the x_1 - x_2 plane (see **Fig.1(a)**). Here, we consider an incident Love wave propagating in the x_1 -direction, which interacts with the cavity generating forward- scattered and back-scattered surface wave.

By virtue of linear superposition principle, the total field in the flawed structure defined by Fig.1(a) can be considered as the superposition of the incident and the scattered waves. The incident wave can be treated in the intact (or reference) structure without cavity, as shown by Fig.1(b), and the scattered field is analyzed in the flawed configuration in Fig.1(c). The scattered field is equivalent to the field generated by the contribution of the tractions exerted on the actual surface of the cavity. Furthermore, these tractions are equal in magnitude but opposite in sign to the corresponding tractions produced by the incident Love wave field on the surface of the fictitious cavity as shown by Fig.1(b). Thus, these tractions can be obtained by calculating the stress components and the outward normal vectors along the fictitious cavity surface using the Cauchy's formula from the incident field. The dynamic reciprocal theorem is then applied to calculate the scattered wave field equivalent to the radiated field generated by these tractions.

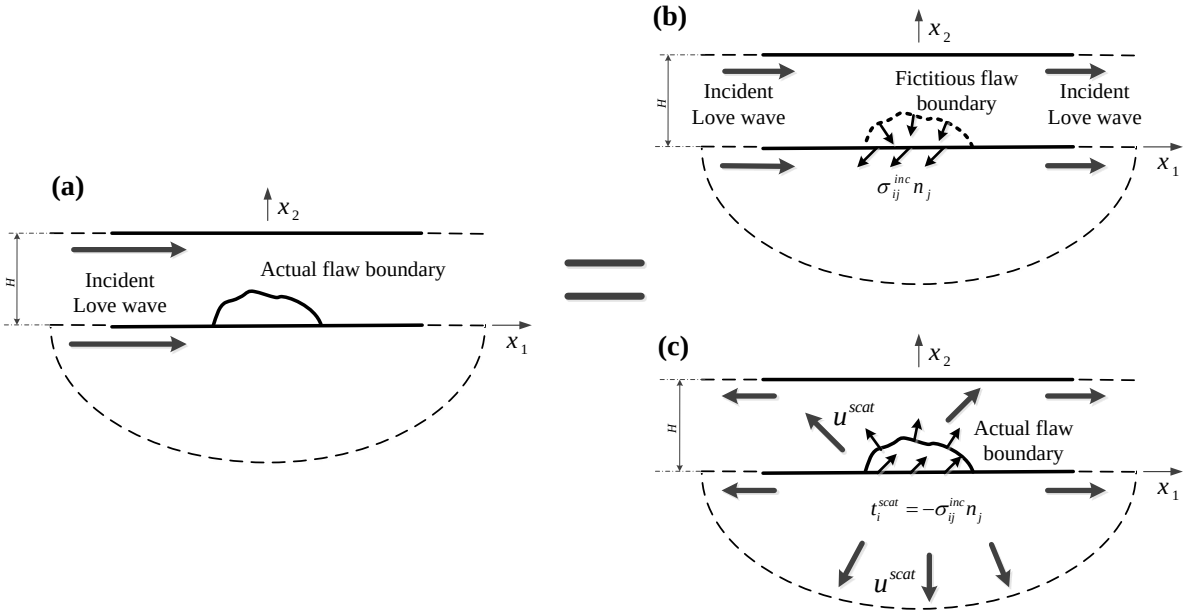

Fig. 1. Linear superposition principle: (a) the total field; (b) the incident field; (c) the scattered field.

3. Equations

3.1. The elasto-dynamic reciprocal theorem

The dynamic reciprocal theorem relates two elasto-dynamic states 1 and 2 of the same bounded or unbounded body, which can be stated as

$$\int_V \left[f_k^1(\boldsymbol{x},\omega) u_k^2(\boldsymbol{x},\omega) - f_k^2(\boldsymbol{x},\omega) u_k^1(\boldsymbol{x},\omega) \right] dV(\boldsymbol{x}) = \int_A \left[\tau_{kl}^2(\boldsymbol{x},\omega) n_k u_l^1(\boldsymbol{x},\omega) - \tau_{kl}^1(\boldsymbol{x},\omega) n_k u_l^2(\boldsymbol{x},\omega) \right] dA(\boldsymbol{x}) \tag{1}$$

where $f_k^{1,2}$, $u_k^{1,2}$ and $\tau_{kl}^{1,2}$ represent body forces, displacements and stresses, respectively, and $\boldsymbol{n}_k$ is the *k*th

component of unit vector outward surface normal to A.

Let us consider a two-dimensional elasto-dynamic problems in an isotropic half-plane with a different homogeneous and isotropic layer covered with boundary L. The boundary integral equation of anti-plane motion for a source point $\boldsymbol{\xi}$ taken on L, in the absence of body forces, is developed from Equation (1) and derived as

$$\frac{1}{2}u(\boldsymbol{\xi},\omega)=\int_L\left[u^*(\boldsymbol{\xi},\boldsymbol{x},\omega)t(\boldsymbol{x},\omega)-t^*(\boldsymbol{\xi},\boldsymbol{x},\omega)u(\boldsymbol{x},\omega)\right]dL(\boldsymbol{x}) \tag{2}$$

Where the factor 1/2 is valid only if the boundary L is smooth at point $\boldsymbol{\xi}$, u^* and t^* are the full-space frequency domain elastodynamic anti-plane fundamental solution displacement and traction tensors, respectively, which are derived [18] as

$$\begin{aligned}
&u^*(\boldsymbol{\xi},\boldsymbol{x},\omega)=\frac{\mathrm{i}}{4\mu_I}H_0^{(1)}\left(k_T^B r\right)\ \left(0\le\xi_2\le H\right)\ \text{ or }\ \frac{\mathrm{i}}{4\mu_{II}}H_0^{(1)}\left(k_T^A r\right)\ \left(\xi_2\le 0\right)\\
&t^*(\boldsymbol{\xi},\boldsymbol{x},\omega)=-\frac{\mathrm{i}k_T^B}{4}H_1^{(1)}\left(k_T^B r\right)\frac{\partial r}{\partial n}\ \left(0\le\xi_2\le H\right)\ \text{ or }\ -\frac{\mathrm{i}k_T^A}{4}H_1^{(1)}\left(k_T^A r\right)\frac{\partial r}{\partial n}\ \left(\xi_2\le 0\right)
\end{aligned} \tag{3}$$

where $H_n^{(1)}(\ )$ is the Hankel function of the nth order of the first kind; μ_A, μ_B, k_T^A, and k_T^B stand for the elastic constants and the wave-numbers of the shear wave at current frequency, for the upper and lower materials, respectively, where $k_T^J=\omega/\sqrt{\mu_J/\rho_J}\,(J=A,B)$, in which ρ_A and ρ_B are material densities; r represents the distance between $\boldsymbol{\xi}$ and $\boldsymbol{x}$; u^* and t^* are the displacement and boundary traction, respectively, at the point $\boldsymbol{x}$, respectively, due to a unit line force exerted at $\boldsymbol{\xi}$. For current anti-plane problem, both the line force and Green's function -- u^* and t^* only have the x_3 component.

Let us assume that, except the flaw region L_1 and L_5, both the free-traction surface and the interface are flat. Let L_0 and L_3 be the free upper surface and the interface between upper-layer and half-plane, respectively, and L_∞^a, L_∞^b represent the remaining infinite part of upper and lower boundary, respectively, which will be omitted by truncation in traditional BEM (see Fig.1).

By substituting all boundaries divided in Fig.2 into Eq.(2), the BIE of the layered media and half-plane are derived as:

$$\begin{aligned}
&\frac{1}{2}u(\boldsymbol{\xi},\omega)+\int_{L_0\cap L_3\cap L_1}t^B(\boldsymbol{\xi},\boldsymbol{x},\omega)u(\boldsymbol{x},\omega)dL(\boldsymbol{x})\\
&+\left(\int_{L_\infty^a\cup L_\infty^b}t^B(\boldsymbol{\xi},\boldsymbol{x},\omega)u(\boldsymbol{x},\omega)dL(\boldsymbol{x})-\int_{L_\infty^a}u^B(\boldsymbol{\xi},\boldsymbol{x},\omega)t(\boldsymbol{x},\omega)dL(\boldsymbol{x})\right)\\
&=\int_{L_3\cap L_1}u^B(\boldsymbol{\xi},\boldsymbol{x},\omega)t(\boldsymbol{x},\omega)dL(\boldsymbol{x})
\end{aligned} \tag{4}$$

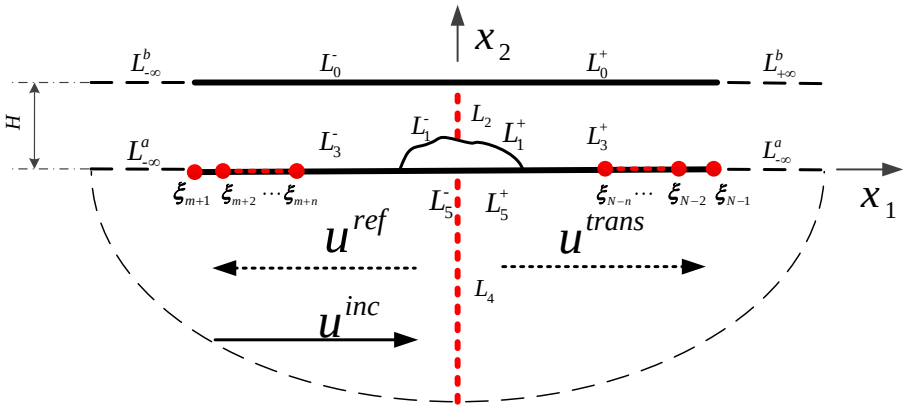

Fig. 2. Schematic definition of the computational domain of the Love-wave scattered field, with divided interface boundaries

$$L = L_{\pm\infty}^{b} \cup L_0^{\pm} \cup L_3^{\pm} \cup L_1^{\pm} \cup L_5^{\pm} \cup L_{\pm\infty}^{a}.$$

and

$$\begin{aligned}
&\frac{1}{2}u(\boldsymbol{\xi},\omega) + \int_{L_3 \cap L_5} t^A(\boldsymbol{\xi},\boldsymbol{x},\omega)u(\boldsymbol{x},\omega)dL(\boldsymbol{x}) \\
&+ \int_{L_{\infty}^{a}} \left(t^A(\boldsymbol{\xi},\boldsymbol{x},\omega)u(\boldsymbol{x},\omega) - u^A(\boldsymbol{\xi},\boldsymbol{x},\omega)t(\boldsymbol{x},\omega) \right) dL(\boldsymbol{x}) \\
&= \int_{L_3 \cap L_5} u^A(\boldsymbol{\xi},\boldsymbol{x},\omega)t(\boldsymbol{x},\omega)dL(\boldsymbol{x})
\end{aligned} \tag{5}$$

respectively, where the superscript A and B indicate the green functions of half-plane and the layer respectively.

3.2. Far-field assumption

Since that body waves geometrically attenuate in the propagating direction, the far-field displacement solution can be approximated by a series of Love surface waves, neglecting the contribution of body waves.

Therefore, we assume that if the truncated points are located far enough from the source regions, the displacement solutions of the infinite boundary at each side can be expressed as:

$$\begin{aligned}
&\text{For} \quad \boldsymbol{x} \in L_{-\infty}^{a} \cup L_{-\infty}^{b}: \\
&u(\boldsymbol{x},\omega) \approx R_1^{-}(\omega)u^{1-}(\boldsymbol{x},\omega) + R_2^{-}(\omega)u^{2-}(\boldsymbol{x},\omega) + \cdots + R_n^{-}(\omega)u^{n-}(\boldsymbol{x},\omega) \\
&\text{For} \quad \boldsymbol{x} \in L_{+\infty}^{a} \cup L_{+\infty}^{b}: \\
&u(\boldsymbol{x},\omega) \approx R_1^{+}(\omega)u^{1+}(\boldsymbol{x},\omega) + R_2^{+}(\omega)u^{2+}(\boldsymbol{x},\omega) + \cdots + R_n^{+}(\omega)u^{n+}(\boldsymbol{x},\omega)
\end{aligned} \tag{6}$$

where the coordinate vector $\boldsymbol{x}$ is form of $(x_1\ x_2)$, $R_i^{\pm}(\omega)$ are defined as the unknown complex amplitudes of the far-field solutions of the *i*th order mode Love wave. Here, n is the number of modes, and $u^{i\pm}(\boldsymbol{x},\omega)$ represent the *i*th order mode displacement of unit amplitude Love wave propagating in the positive and negative direction of axis x_1. (Note that Love surface waves are dispersive.)

By virtue of assumptions in Eq.(6), Eq.(4) and Eq.(5) can be rewritten as:

$$\begin{aligned}
&\frac{1}{2}u(\boldsymbol{\xi},\omega) + \int_{L_0 \cap L_3 \cap L_1} t^B(\boldsymbol{\xi},\boldsymbol{x},\omega)u(\boldsymbol{x},\omega)dL(\boldsymbol{x}) - \int_{L_3 \cap L_1} u^B(\boldsymbol{\xi},\boldsymbol{x},\omega)t(\boldsymbol{x},\omega)dL(\boldsymbol{x}) \\
&= \sum_i \begin{aligned}[t] & R_i^{-}\left[\int_{L_{-\infty}^{a} \cup L_{-\infty}^{b}} t^B(\boldsymbol{\xi},\boldsymbol{x},\omega)u^{i-}(\boldsymbol{x},\omega)dL(\boldsymbol{x}) - \int_{L_{-\infty}^{a}} u^B(\boldsymbol{\xi},\boldsymbol{x},\omega)t^{i-}(\boldsymbol{x},\omega)dL(\boldsymbol{x}) \right] \\ & + R_i^{+}\left[\int_{L_{+\infty}^{a} \cup L_{+\infty}^{b}} t^B(\boldsymbol{\xi},\boldsymbol{x},\omega)u^{i+}(\boldsymbol{x},\omega)dL(\boldsymbol{x}) - \int_{L_{+\infty}^{a}} u^B(\boldsymbol{\xi},\boldsymbol{x},\omega)t^{i+}(\boldsymbol{x},\omega)dL(\boldsymbol{x}) \right] \end{aligned} \\
&(i = 1, 2, \cdots, n)
\end{aligned} \tag{7}$$

and

$$\begin{aligned}
&\frac{1}{2}u(\boldsymbol{\xi},\omega) + \int_{L_3 \cap L_1} t^A(\boldsymbol{\xi},\boldsymbol{x},\omega)u(\boldsymbol{x},\omega)dL(\boldsymbol{x}) - \int_{L_3 \cap L_1} u^A(\boldsymbol{\xi},\boldsymbol{x},\omega)t(\boldsymbol{x},\omega)dL(\boldsymbol{x}) \\
&= -\sum_i \begin{aligned}[t] & R_i^{-}\left[\int_{L_{-\infty}^{a}} t^A(\boldsymbol{\xi},\boldsymbol{x},\omega)u^{i-}(\boldsymbol{x},\omega)dL(\boldsymbol{x}) - \int_{L_{-\infty}^{a}} u^A(\boldsymbol{\xi},\boldsymbol{x},\omega)t^{i-}(\boldsymbol{x},\omega)dL(\boldsymbol{x}) \right] \\ & + R_i^{+}\left[\int_{L_{+\infty}^{a}} t^A(\boldsymbol{\xi},\boldsymbol{x},\omega)u^{i+}(\boldsymbol{x},\omega)dL(\boldsymbol{x}) - \int_{L_{+\infty}^{a}} u^A(\boldsymbol{\xi},\boldsymbol{x},\omega)t^{i+}(\boldsymbol{x},\omega)dL(\boldsymbol{x}) \right] \end{aligned} \\
&(i = 1, 2, \cdots, n)
\end{aligned} \tag{8}$$

respectively. From Eq.(7) and Eq.(8), we define:

$$A_i^{B\pm}(\boldsymbol{\xi}) = \int_{L_{\pm\infty}^{a} \cup L_{\pm\infty}^{b}} t^B(\boldsymbol{\xi},\boldsymbol{x},\omega)u^{i\pm}(\boldsymbol{x},\omega)dL(\boldsymbol{x}) - \int_{L_{\pm\infty}^{a}} u^B(\boldsymbol{\xi},\boldsymbol{x},\omega)t^{i\pm}(\boldsymbol{x},\omega)dL(\boldsymbol{x}) \tag{9}$$

and

$$A_i^{A\pm}(\boldsymbol{\xi})=\int_{L_{\pm\infty}^a} t^A(\boldsymbol{\xi},\boldsymbol{x},\omega)u^{i\pm}(\boldsymbol{x},\omega)dL(\boldsymbol{x})-\int_{L_{\pm\infty}^a} u^A(\boldsymbol{\xi},\boldsymbol{x},\omega)t^{i\pm}(\boldsymbol{x},\omega)dL(\boldsymbol{x}) \tag{10}$$

which represent the corrected items accounting for the contribution of the omitted boundary. Thus, Eq.(7) and (8) are simplified as:

$$\begin{aligned}&\frac{1}{2}u(\boldsymbol{\xi},\omega)+\int_{L_0\cap L_3\cap L_1} t^B(\boldsymbol{\xi},\boldsymbol{x},\omega)u(\boldsymbol{x},\omega)dL(\boldsymbol{x})-\int_{L_3\cap L_1} u^B(\boldsymbol{\xi},\boldsymbol{x},\omega)t(\boldsymbol{x},\omega)dL(\boldsymbol{x})\\&=\sum_i\left(R_i^- A_i^{B-}+R_i^+ A_i^{B+}\right)\quad(i=1,2,\cdots,n)\end{aligned} \tag{11}$$

$$\begin{aligned}&\frac{1}{2}u(\boldsymbol{\xi},\omega)+\int_{L_3\cap L_1} t^A(\boldsymbol{\xi},\boldsymbol{x},\omega)u(\boldsymbol{x},\omega)dL(\boldsymbol{x})-\int_{L_3\cap L_1} u^A(\boldsymbol{\xi},\boldsymbol{x},\omega)t(\boldsymbol{x},\omega)dL(\boldsymbol{x})\\&+\sum_i\left(R_i^- A_i^{A-}+R_i^+ A_i^{A+}\right)=\int_{L_3} u^A(\boldsymbol{\xi},\boldsymbol{x},\omega)t(\boldsymbol{x},\omega)dL(\boldsymbol{x})\qquad(i=1,2,\cdots,n)\end{aligned} \tag{12}$$

Note that $2n$ unknown parameters $R_i^{\pm}(\omega)$ are introduced into the BIEs, which will add degrees of freedom to the final BEM system of the BIEs.

3.3. Correction over the omitted part of the infinite boundary

In traditional BEM approaches, the contribution of integral terms on the infinite boundary, i.e. the fourth term on the right hand side of Eq.(4) and the third term on the right hand side of Eq.(5), are omitted, which introduces considerable error. In order to separately determine the integral terms over infinite boundaries such as $L_{\pm\infty}^a$ and $L_{\pm\infty}^b$, a multi-domain approach is applied, which involves the division of the whole interfaces and boundaries into four regions by introducing two fictitious boundaries L_2 and L_4, as shown in Fig.2. Here, an incident Love wave mode with unit amplitude is introduced propagating along the upper free surface in the positive or negative direction of x_1, respectively (see Fig.3).

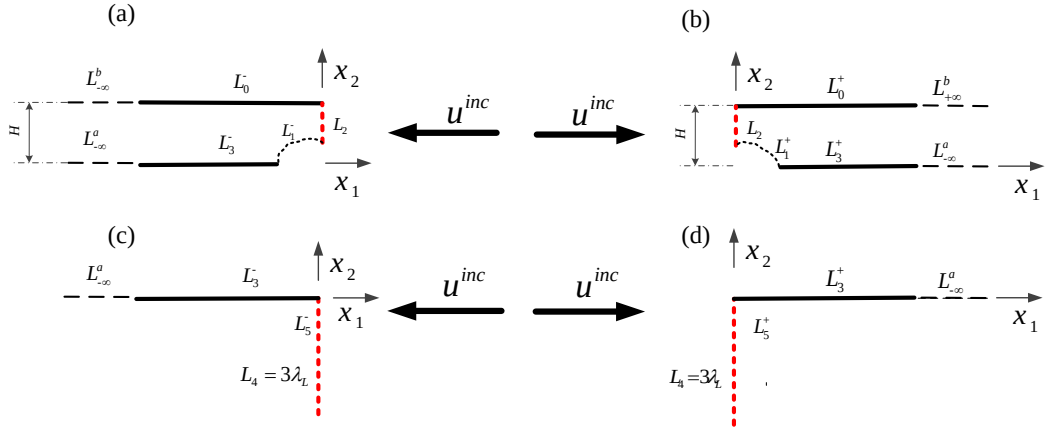

Fig. 3. Schematic diagram of the multi-domain approach: (a) calculate A_i^{B-}; (b) calculate A_i^{B+}; (c) calculate A_i^{A-}; (d) calculate A_i^{A+};

Let us choose the Love surface wave of unit amplitude as elastodynamic state 1 and the full-space fundamental solution as elasto-dynamic state 2. For instance, by virtue of reciprocal theorem seen from Eq.(2), the BIE for region 1 is given as:

$$\frac{1}{2}u^{i\pm}(\boldsymbol{\xi},\omega)=\int_L\left[u^*(\boldsymbol{\xi},\boldsymbol{x},\omega)t^{i\pm}(\boldsymbol{x},\omega)-t^*(\boldsymbol{\xi},\boldsymbol{x},\omega)u^{i\pm}(\boldsymbol{x},\omega)\right]dL(\boldsymbol{x}) \tag{13}$$

By simplifying Eq.(13), we arrive at:

$$\begin{aligned}A_i^{B+}(\boldsymbol{\xi})=&-\frac{1}{2}u^{i+}(\boldsymbol{\xi},\omega)-\int_{L_0^+\cup L_1^+\cup L_3^+\cup L_2} t^B(\boldsymbol{\xi},\boldsymbol{x},\omega)u^{i+}(\boldsymbol{x},\omega)dL(\boldsymbol{x})\\&+\int_{L_1^+\cup L_3^+\cup L_2} u^B(\boldsymbol{\xi},\boldsymbol{x},\omega)t^{i+}(\boldsymbol{x},\omega)dL(\boldsymbol{x})\end{aligned} \tag{14}$$

By implying an analogous approach for other regions, we can get $A_i^{B-}(\boldsymbol{\xi})$, $A_i^{A-}(\boldsymbol{\xi})$ and $A_i^{A+}(\boldsymbol{\xi})$, which are expressed as:

$$A_i^{B-}(\boldsymbol{\xi}) = -\frac{1}{2}u^{i-}(\boldsymbol{\xi},\omega) - \int_{L_0^-\cup L_1^-\cup L_3^-\cup L_2} t^B(\boldsymbol{\xi},\boldsymbol{x},\omega)u^{i-}(\boldsymbol{x},\omega)dL(\boldsymbol{x}) + \int_{L_1^-\cup L_3^-\cup L_2} u^B(\boldsymbol{\xi},\boldsymbol{x},\omega)t^{i-}(\boldsymbol{x},\omega)dL(\boldsymbol{x}) \tag{15}$$

$$A_i^{A-}(\boldsymbol{\xi}) = -\frac{1}{2}u^{i-}(\boldsymbol{\xi},\omega) - \int_{L_3^-\cup L_5^-\cup L_4} t^A(\boldsymbol{\xi},\boldsymbol{x},\omega)u^{i-}(\boldsymbol{x},\omega)dL(\boldsymbol{x}) + \int_{L_3^-\cup L_5^-\cup L_4} u^A(\boldsymbol{\xi},\boldsymbol{x},\omega)t^{i-}(\boldsymbol{x},\omega)dL(\boldsymbol{x}) \tag{16}$$

$$A_i^{A+}(\boldsymbol{\xi}) = -\frac{1}{2}u^{i+}(\boldsymbol{\xi},\omega) - \int_{L_3^+\cup L_5^+\cup L_4} t^A(\boldsymbol{\xi},\boldsymbol{x},\omega)u^{i+}(\boldsymbol{x},\omega)dL(\boldsymbol{x}) + \int_{L_3^+\cup L_5^+\cup L_4} u^A(\boldsymbol{\xi},\boldsymbol{x},\omega)t^{i+}(\boldsymbol{x},\omega)dL(\boldsymbol{x}) \tag{17}$$

Note that for the calculation of $A_i^{B-}(\boldsymbol{\xi})$ and $A_i^{A-}(\boldsymbol{\xi})$, the incident Love wave is assumed to propagate in the positive direction, while for $A_i^{A+}(\boldsymbol{\xi})$ and $A_i^{B+}(\boldsymbol{\xi})$ the propagating direction is opposite. The fictitious boundary L_4 is, in principle, infinite. However, since the integrand over L_4 attenuate rapidly in exponential form away from the interface of half-plane, without loss of accuracy, we consider the boundary L_4 as a distance of about two Love wavelength.

4. Numerical computation

Numerical solutions of Eq.(11) and Eq.(12) require the discretization of the boundary L_i into elements. After the discretization of the boundary and interpolation of the displacements and tractions, the discretized BIEs for the layer and half-plane can be written for each node $\boldsymbol{\xi}_j$ and $\boldsymbol{\upsilon}_j$ respectively as

$$\frac{1}{2}u(\boldsymbol{\xi}_j,\omega) + \sum_{e\in L_0\cup L_1\cup L_3}\sum_{k=1}^{N_e}\left\{\int_{L_e} t^B(\boldsymbol{\xi}_j,\eta,\omega)\phi_k(\eta)\mathrm{d}L(\eta)\right\}u(\boldsymbol{\xi}_k,\omega) + \sum_{i=1}^{n}A_i^{B-}(\boldsymbol{\xi}_j)R_i^-(\omega) + \sum_{i=1}^{n}A_i^{B+}(\boldsymbol{\xi}_j)R_i^+(\omega) = \sum_{e\in L_1\cup L_3}\sum_{k=1}^{N_e}\left\{\int_{L_e} u^B(\boldsymbol{\xi}_j,\eta,\omega)\phi_k(\eta)\mathrm{d}L(\eta)\right\}t(\boldsymbol{\xi}_j,\omega) \quad j=1,2,\cdots,N_1 \tag{18}$$

and

$$\frac{1}{2}u(\boldsymbol{\upsilon}_j,\omega) + \sum_{e\in L_3}\sum_{k=1}^{N_e}\left\{\int_{\Gamma_e} t^A(\boldsymbol{\upsilon}_j,\eta,\omega)\phi_k(\eta)\mathrm{d}L(\eta)\right\}u(\boldsymbol{\upsilon}_k,\omega) + \sum_{i=1}^{n}A_i^{A-}(\boldsymbol{\xi}_j)R_i^-(\omega) + \sum_{i=1}^{n}A_i^{A+}(\boldsymbol{\xi}_j)R_i^+(\omega) = \sum_{e\in L_3}\sum_{k=1}^{N_e}\left\{\int_{L_e} u^A(\boldsymbol{\upsilon}_j,\eta,\omega)\phi_k(\eta)\mathrm{d}L(\eta)\right\}t(\boldsymbol{\xi}_k,\omega) \quad j=1,2,\cdots,N_2 \tag{19}$$

where N_1, N_2 are the total number of nodes for the layer and half-plane respectively, N_e is the number of nodes per element, ϕ_k is the same shape function for each element and $\eta\in[-1,1]$ represents the intrinsic co-ordinate of the parent element. It is noted that the calculation of corrected coefficients $A_i^{B\pm}(\boldsymbol{\xi})$ and $A_i^{A\pm}(\boldsymbol{\xi})$ is performed in the previous section.

Eq.(18) and Eq.(19) can be expressed in a more concise manner by defining：

$$T_{jk}^{B}=\begin{cases}\int_{L_e} t^{B}\left(\boldsymbol{\xi}_j,\eta,\omega\right)\phi_k\left(\eta\right)dL\left(\eta\right) & j\neq k\\ \int_{L_e} t^{B}\left(\boldsymbol{\xi}_j,\eta,\omega\right)\phi_k\left(\eta\right)dL\left(\eta\right)+\dfrac{1}{2} & j=k\end{cases}$$
$$G_{jk}^{B}=\int_{L_e} u^{B}\left(\boldsymbol{\xi}_j,\eta,\omega\right)\phi_k\left(\eta\right)dL\left(\eta\right) \tag{20}$$

and

$$T_{jk}^{A}=\begin{cases}\int_{L_e} t^{A}\left(\boldsymbol{\upsilon}_j,\eta,\omega\right)\phi_k\left(\eta\right)dL\left(\eta\right) & j\neq k\\ \int_{L_e} t^{A}\left(\boldsymbol{\upsilon}_j,\eta,\omega\right)\phi_k\left(\eta\right)dL\left(\eta\right)+\dfrac{1}{2} & j=k\end{cases}$$
$$G_{jk}^{A}=\int_{L_e} u^{A}\left(\boldsymbol{\upsilon}_j,\eta,\omega\right)\phi_k\left(\eta\right)dL\left(\eta\right) \tag{21}$$

where the subscripts represent the collocation point $\boldsymbol{\xi}_j$ and $\boldsymbol{\upsilon}_j$ with the node k of element e. Then the above equations are rewritten as:

$$\begin{aligned}&\sum_{e\in L_0\cup L_1\cup L_3}\sum_{k=1}^{N_e}T_{jk}^{B}u\left(\boldsymbol{\xi}_j,\omega\right)+\sum_{i=1}^{n}A_i^{B-}\left(\boldsymbol{\xi}_j\right)R_i^{-}\left(\omega\right)+\sum_{i=1}^{n}A_i^{B+}\left(\boldsymbol{\xi}_j\right)R_i^{+}\left(\omega\right)\\&=\sum_{e\in L_1\cup L_3}\sum_{k=1}^{N_e}G_{jk}^{B}t\left(\boldsymbol{\xi}_j,\omega\right)\quad j=1,2,\cdots,N_1\end{aligned} \tag{22}$$

and

$$\begin{aligned}&\sum_{e\in L_3}\sum_{k=1}^{N_e}T_{jk}^{A}u\left(\boldsymbol{\upsilon}_k,\omega\right)+\sum_{i=1}^{n}A_i^{A-}\left(\boldsymbol{\upsilon}_j\right)R_i^{-}\left(\omega\right)+\sum_{i=1}^{n}A_i^{A+}\left(\boldsymbol{\upsilon}_j\right)R_i^{+}\left(\omega\right)\\&=\sum_{e\in L_3}\sum_{k=1}^{N_e}G_{jk}^{A}t\left(\boldsymbol{\upsilon}_k,\omega\right)\quad j=1,2,\cdots,N_2\end{aligned} \tag{23}$$

Then, let us assemble the local element T_{jk}^{B}, G_{jk}^{B} into global matrices $\boldsymbol{H}^{B}$, $\boldsymbol{G}^{B}$, the node displacement $u\left(\boldsymbol{\xi}_j,\omega\right)$, node traction $t\left(\boldsymbol{\xi}_j,\omega\right)$ into global matrices $\boldsymbol{U}^{B}$, $\boldsymbol{T}^{B}$, and the correction $A_i^{B\pm}\left(\boldsymbol{\xi}_j\right)$, the unknown amplitudes $R_i^{\pm}\left(\omega\right)$ into the correction matrices $\boldsymbol{A}^{B\pm}$, the amplitude matrices $\boldsymbol{R}^{\pm}$. Eq.(22) can be written as:

$$\boldsymbol{H}^{B}\boldsymbol{U}^{B}+\boldsymbol{A}^{B\pm}\boldsymbol{R}^{\pm}=\boldsymbol{G}^{B}\boldsymbol{T}^{B} \tag{24}$$

where,

$$\begin{aligned}\boldsymbol{U}^{B}&=\left[u\left(\boldsymbol{\xi}_1,\omega\right)\quad u\left(\boldsymbol{\xi}_2,\omega\right)\quad\cdots\quad u\left(\boldsymbol{\xi}_{N_1},\omega\right)\right]^{T}\\\boldsymbol{T}^{B}&=\left[t\left(\boldsymbol{\xi}_1,\omega\right)\quad t\left(\boldsymbol{\xi}_2,\omega\right)\quad\cdots\quad t\left(\boldsymbol{\xi}_{N_1},\omega\right)\right]^{T}\end{aligned} \tag{25}$$

$$\boldsymbol{A}^{B\pm}=\begin{bmatrix}A_1^{B\pm}\left(\boldsymbol{\xi}_1\right) & A_2^{B\pm}\left(\boldsymbol{\xi}_1\right) & \cdots & A_n^{B\pm}\left(\boldsymbol{\xi}_1\right)\\ A_1^{B\pm}\left(\boldsymbol{\xi}_2\right) & A_2^{B\pm}\left(\boldsymbol{\xi}_2\right) & \cdots & A_n^{B\pm}\left(\boldsymbol{\xi}_2\right)\\ \vdots & \vdots & \vdots & \vdots\\ A_1^{B\pm}\left(\boldsymbol{\xi}_{N_1}\right) & A_2^{B\pm}\left(\boldsymbol{\xi}_{N_1}\right) & \cdots & A_n^{B\pm}\left(\boldsymbol{\xi}_{N_1}\right)\end{bmatrix} \tag{26}$$

$$\boldsymbol{R}^{\pm}=\left[R_1^{\pm}\left(\omega\right)\quad R_2^{\pm}\left(\omega\right)\quad\cdots\quad R_n^{\pm}\left(\omega\right)\right]^{T} \tag{27}$$

Conveniently, the corrected BEM system can be rewritten as:

$$\begin{bmatrix}\boldsymbol{T}_{11}^{B} & \boldsymbol{T}_{12}^{B} & \boldsymbol{T}_{13}^{B} & \boldsymbol{T}_{14}^{B}\\ \boldsymbol{T}_{21}^{B} & \boldsymbol{T}_{22}^{B} & \boldsymbol{T}_{23}^{B} & \boldsymbol{T}_{24}^{B}\\ \boldsymbol{T}_{31}^{B} & \boldsymbol{T}_{32}^{B} & \boldsymbol{T}_{33}^{B} & \boldsymbol{T}_{34}^{B}\\ \boldsymbol{T}_{41}^{B} & \boldsymbol{T}_{42}^{B} & \boldsymbol{T}_{43}^{B} & \boldsymbol{T}_{44}^{B}\end{bmatrix}\begin{bmatrix}\boldsymbol{U}_0\\ \boldsymbol{U}_3^{-}\\ \boldsymbol{U}_1\\ \boldsymbol{U}_3^{+}\end{bmatrix}+\boldsymbol{A}^{B\pm}\boldsymbol{R}^{\pm}=\begin{bmatrix}\boldsymbol{G}_{11}^{B} & \boldsymbol{G}_{12}^{B} & \boldsymbol{G}_{13}^{B} & \boldsymbol{G}_{14}^{B}\\ \boldsymbol{G}_{21}^{B} & \boldsymbol{G}_{22}^{B} & \boldsymbol{G}_{23}^{B} & \boldsymbol{G}_{24}^{B}\\ \boldsymbol{G}_{31}^{B} & \boldsymbol{G}_{32}^{B} & \boldsymbol{G}_{33}^{B} & \boldsymbol{G}_{34}^{B}\\ \boldsymbol{G}_{41}^{B} & \boldsymbol{G}_{42}^{B} & \boldsymbol{G}_{43}^{B} & \boldsymbol{G}_{44}^{B}\end{bmatrix}\begin{bmatrix}\boldsymbol{T}_0\\ \boldsymbol{T}_3^{-}\\ \boldsymbol{T}_1\\ \boldsymbol{T}_3^{+}\end{bmatrix} \tag{28}$$

where $\boldsymbol{T}_{ij}^{B}$, $\boldsymbol{G}_{ij}^{B}$ are block matrices of $\boldsymbol{T}^{B}$, $\boldsymbol{G}^{B}$, and $\boldsymbol{U}_{\alpha}^{\pm}$, $\boldsymbol{T}_{\alpha}^{\pm}$ are the node displacement vectors and node traction vectors corresponding to $L_{\alpha}^{\pm}$, respectively.

Analogously, Eq.(23) can be expressed in matrix form:

$$\boldsymbol{H}^A\boldsymbol{U}^A+\boldsymbol{A}^{A\pm}\boldsymbol{R}^{\pm}=\boldsymbol{G}^A\boldsymbol{T}^A \tag{29}$$

where,

$$\begin{aligned}\boldsymbol{U}^A&=\left[u\left(\boldsymbol{\upsilon}_1,\omega\right)\quad u\left(\boldsymbol{\upsilon}_2,\omega\right)\quad\cdots\quad u\left(\boldsymbol{\upsilon}_{N_2},\omega\right)\right]^T\\ \boldsymbol{T}^A&=\left[t\left(\boldsymbol{\upsilon}_1,\omega\right)\quad t\left(\boldsymbol{\upsilon}_2,\omega\right)\quad\cdots\quad t\left(\boldsymbol{\upsilon}_{N_2},\omega\right)\right]^T\end{aligned} \tag{30}$$

$$\boldsymbol{A}^{A\pm}=\begin{bmatrix}A_1^{A\pm}\left(\boldsymbol{\upsilon}_1\right) & A_2^{A\pm}\left(\boldsymbol{\upsilon}_1\right) & \cdots & A_n^{A\pm}\left(\boldsymbol{\upsilon}_1\right)\\ A_1^{A\pm}\left(\boldsymbol{\upsilon}_2\right) & A_2^{A\pm}\left(\boldsymbol{\upsilon}_2\right) & \cdots & A_n^{A\pm}\left(\boldsymbol{\upsilon}_2\right)\\ \vdots & \vdots & \vdots & \vdots\\ A_1^{A\pm}\left(\boldsymbol{\upsilon}_{N_1}\right) & A_2^{A\pm}\left(\boldsymbol{\upsilon}_{N_1}\right) & \cdots & A_n^{A\pm}\left(\boldsymbol{\upsilon}_{N_1}\right)\end{bmatrix} \tag{31}$$

and

$$\begin{bmatrix}\boldsymbol{T}_{11}^A & \boldsymbol{T}_{12}^A & \boldsymbol{T}_{13}^A\\ \boldsymbol{T}_{21}^A & \boldsymbol{T}_{22}^A & \boldsymbol{T}_{23}^A\\ \boldsymbol{T}_{31}^A & \boldsymbol{T}_{32}^A & \boldsymbol{T}_{33}^A\end{bmatrix}\begin{bmatrix}\boldsymbol{U}_3^-\\ \boldsymbol{U}_5\\ \boldsymbol{U}_3^+\end{bmatrix}+\boldsymbol{A}^{A\pm}\boldsymbol{R}^{\pm}=\begin{bmatrix}\boldsymbol{G}_{11}^A & \boldsymbol{G}_{12}^A & \boldsymbol{G}_{13}^A\\ \boldsymbol{G}_{21}^A & \boldsymbol{G}_{22}^A & \boldsymbol{G}_{23}^A\\ \boldsymbol{G}_{31}^A & \boldsymbol{G}_{32}^A & \boldsymbol{G}_{33}^A\end{bmatrix}\begin{bmatrix}\boldsymbol{T}_3^-\\ \boldsymbol{T}_5\\ \boldsymbol{T}_3^+\end{bmatrix} \tag{32}$$

where $\boldsymbol{T}_{ij}^B$, $\boldsymbol{G}_{ij}^B$ are block matrices of $\boldsymbol{T}^B$, $\boldsymbol{G}^B$, and $\boldsymbol{U}_\alpha^{\pm}$, $\boldsymbol{T}_\alpha^{\pm}$ are the node displacement vectors and node traction vectors corresponding to $L_\alpha^{\pm}$, respectively.

It should be pointed out that the unknown coefficient matrices $\boldsymbol{R}^{\pm}$ which are assembled into the modified BEM system (Eq.(24) and Eq.(29)), will add $2n$ degrees of freedom into the final BEM system of equations. Here, we propose a modified method for Love wave multi-mode by introducing finite sequence truncated points on far-field regions. Based on the far-field assumption (Eq.(6)), far-field displacements of $2n$ sequence points $\boldsymbol{\xi}_{m+i}\left(i=1,2,\cdots,n\right)$ and $\boldsymbol{\xi}_{N+i-1}\left(i=1,2,\cdots,n\right)$ (see as Fig.1) are written as:

$$\begin{aligned}u\left(\boldsymbol{\xi}_{m+i},\omega\right)&=\sum_{j=1}^{n}u^{j-}\left(\boldsymbol{\xi}_{m+i},\omega\right)R_j^-\left(\omega\right)\\ u\left(\boldsymbol{\xi}_{N+i-1},\omega\right)&=\sum_{j=1}^{n}u^{j+}\left(\boldsymbol{\xi}_{N+i-1},\omega\right)R_j^+\left(\omega\right)\quad\left(i=1,2,\cdots,n\right)\end{aligned} \tag{33}$$

which can also be expressed as the form of matrix:

$$\boldsymbol{I}_R^-\boldsymbol{U}_3^-=\boldsymbol{U}_R^-\boldsymbol{R}^- \tag{34}$$

where,

$$\boldsymbol{I}_R^-=\begin{bmatrix}-\boldsymbol{I}_n & \boldsymbol{0}\\ \boldsymbol{0} & \boldsymbol{0}\end{bmatrix} \tag{35}$$

$$\boldsymbol{U}_R^-=\begin{bmatrix}u^{1-}\left(\boldsymbol{\xi}_{m+1},\omega\right) & u^{2-}\left(\boldsymbol{\xi}_{m+1},\omega\right) & \cdots & u^{n-}\left(\boldsymbol{\xi}_{m+1},\omega\right)\\ u^{1-}\left(\boldsymbol{\xi}_{m+2},\omega\right) & u^{2-}\left(\boldsymbol{\xi}_{m+2},\omega\right) & \cdots & u^{n-}\left(\boldsymbol{\xi}_{m+2},\omega\right)\\ \vdots & \vdots & \vdots & \vdots\\ u^{1-}\left(\boldsymbol{\xi}_{m+n},\omega\right) & u^{2-}\left(\boldsymbol{\xi}_{m+n},\omega\right) & \cdots & u^{n-}\left(\boldsymbol{\xi}_{m+n},\omega\right)\end{bmatrix} \tag{36}$$

and

$$\boldsymbol{I}_R^+\boldsymbol{U}_3^+=\boldsymbol{U}_R^+\boldsymbol{R}^+ \tag{37}$$

where,

$$\boldsymbol{I}_R^+=\begin{bmatrix}\boldsymbol{0} & \boldsymbol{0}\\ \boldsymbol{0} & -\boldsymbol{I}_n\end{bmatrix} \tag{38}$$

$$\boldsymbol{U}_R^+=\begin{bmatrix}u^{1+}\left(\boldsymbol{\xi}_{N-n+1},\omega\right) & u^{2+}\left(\boldsymbol{\xi}_{N-n+1},\omega\right) & \cdots & u^{n+}\left(\boldsymbol{\xi}_{N-n+1},\omega\right)\\ u^{1+}\left(\boldsymbol{\xi}_{N-n+2},\omega\right) & u^{2+}\left(\boldsymbol{\xi}_{N-n+2},\omega\right) & \cdots & u^{n+}\left(\boldsymbol{\xi}_{N-n+2},\omega\right)\\ \vdots & \vdots & \vdots & \vdots\\ u^{1+}\left(\boldsymbol{\xi}_N,\omega\right) & u^{2+}\left(\boldsymbol{\xi}_N,\omega\right) & \cdots & u^{n+}\left(\boldsymbol{\xi}_N,\omega\right)\end{bmatrix} \tag{39}$$

Then, by virtue of boundary conditions of two kinds: continuity of displacements and stresses, among the boundary L_3, Eq.(28), Eq.(32) and Eq.(34), Eq.(37) are finally assembled into global BEM system, to obtain the scattering coefficients and displacements directly, thus:

$$
\begin{bmatrix}
\boldsymbol{T}_{11}^{B} & \boldsymbol{T}_{12}^{B} & \boldsymbol{T}_{13}^{B} & \boldsymbol{T}_{14}^{B} & -\boldsymbol{G}_{12}^{B} & \mathbf{0} & -\boldsymbol{G}_{14}^{B} & \boldsymbol{A}_{0}^{B-} & \boldsymbol{A}_{0}^{B+} \\
\boldsymbol{T}_{21}^{B} & \boldsymbol{T}_{22}^{B} & \boldsymbol{T}_{23}^{B} & \boldsymbol{T}_{24}^{B} & -\boldsymbol{G}_{22}^{B} & \mathbf{0} & -\boldsymbol{G}_{24}^{B} & \boldsymbol{A}_{3-}^{B-} & \boldsymbol{A}_{3-}^{B+} \\
\boldsymbol{T}_{31}^{B} & \boldsymbol{T}_{32}^{B} & \boldsymbol{T}_{33}^{B} & \boldsymbol{T}_{34}^{B} & -\boldsymbol{G}_{32}^{B} & \mathbf{0} & -\boldsymbol{G}_{34}^{B} & \boldsymbol{A}_{1}^{B-} & \boldsymbol{A}_{1}^{B+} \\
\boldsymbol{T}_{41}^{B} & \boldsymbol{T}_{42}^{B} & \boldsymbol{T}_{43}^{B} & \boldsymbol{T}_{44}^{B} & -\boldsymbol{G}_{42}^{B} & \mathbf{0} & -\boldsymbol{G}_{44}^{B} & \boldsymbol{A}_{3+}^{B-} & \boldsymbol{A}_{3+}^{B+} \\
\mathbf{0} & \boldsymbol{T}_{11}^{A} & \mathbf{0} & \boldsymbol{T}_{13}^{A} & \boldsymbol{G}_{11}^{A} & \boldsymbol{T}_{12}^{A} & \boldsymbol{G}_{13}^{A} & \boldsymbol{A}_{3-}^{A-} & \boldsymbol{A}_{3-}^{A+} \\
\mathbf{0} & \boldsymbol{T}_{21}^{A} & \mathbf{0} & \boldsymbol{T}_{23}^{A} & \boldsymbol{G}_{21}^{A} & \boldsymbol{T}_{22}^{A} & \boldsymbol{G}_{23}^{A} & \boldsymbol{A}_{5}^{A-} & \boldsymbol{A}_{5}^{A+} \\
\mathbf{0} & \boldsymbol{T}_{31}^{A} & \mathbf{0} & \boldsymbol{T}_{33}^{A} & \boldsymbol{G}_{31}^{A} & \boldsymbol{T}_{32}^{A} & \boldsymbol{G}_{33}^{A} & \boldsymbol{A}_{3+}^{A-} & \boldsymbol{A}_{3+}^{A+} \\
\mathbf{0} & \boldsymbol{I}_{R}^{-} & \mathbf{0} & \mathbf{0} & \mathbf{0} & \mathbf{0} & \mathbf{0} & \boldsymbol{U}_{R}^{-} & \mathbf{0} \\
\mathbf{0} & \mathbf{0} & \mathbf{0} & \boldsymbol{I}_{R}^{+} & \mathbf{0} & \mathbf{0} & \mathbf{0} & \mathbf{0} & \boldsymbol{U}_{R}^{+}
\end{bmatrix}
\begin{bmatrix}
\boldsymbol{U}_{0} \\ \boldsymbol{U}_{3-} \\ \boldsymbol{U}_{1} \\ \boldsymbol{U}_{3+} \\ \boldsymbol{T}_{3-} \\ \boldsymbol{U}_{5} \\ \boldsymbol{T}_{3+} \\ \boldsymbol{R}^{-} \\ \boldsymbol{R}^{+}
\end{bmatrix}
$$

$$
=
\begin{bmatrix}
\boldsymbol{G}_{11}^{B} & \boldsymbol{G}_{12}^{B} & \boldsymbol{G}_{13}^{B} & \boldsymbol{G}_{14}^{B} & \mathbf{0} & \mathbf{0} & \mathbf{0} & \mathbf{0} & \mathbf{0} \\
\boldsymbol{G}_{21}^{B} & \boldsymbol{G}_{22}^{B} & \boldsymbol{G}_{23}^{B} & \boldsymbol{G}_{24}^{B} & \mathbf{0} & \mathbf{0} & \mathbf{0} & \mathbf{0} & \mathbf{0} \\
\boldsymbol{G}_{31}^{B} & \boldsymbol{G}_{32}^{B} & \boldsymbol{G}_{33}^{B} & \boldsymbol{G}_{34}^{B} & \mathbf{0} & \mathbf{0} & \mathbf{0} & \mathbf{0} & \mathbf{0} \\
\boldsymbol{G}_{41}^{B} & \boldsymbol{G}_{42}^{B} & \boldsymbol{G}_{43}^{B} & \boldsymbol{G}_{44}^{B} & \mathbf{0} & \mathbf{0} & \mathbf{0} & \mathbf{0} & \mathbf{0} \\
\mathbf{0} & \mathbf{0} & \mathbf{0} & \boldsymbol{T}_{13}^{A} & \mathbf{0} & \boldsymbol{G}_{12}^{A} & \mathbf{0} & \mathbf{0} & \mathbf{0} \\
\mathbf{0} & \mathbf{0} & \mathbf{0} & \boldsymbol{T}_{23}^{A} & \mathbf{0} & \boldsymbol{G}_{22}^{A} & \mathbf{0} & \mathbf{0} & \mathbf{0} \\
\mathbf{0} & \mathbf{0} & \mathbf{0} & \boldsymbol{T}_{33}^{A} & \mathbf{0} & \boldsymbol{G}_{32}^{A} & \mathbf{0} & \mathbf{0} & \mathbf{0} \\
\mathbf{0} & \mathbf{0} & \mathbf{0} & \mathbf{0} & \mathbf{0} & \mathbf{0} & \mathbf{0} & \mathbf{0} & \mathbf{0} \\
\mathbf{0} & \mathbf{0} & \mathbf{0} & \mathbf{0} & \mathbf{0} & \mathbf{0} & \mathbf{0} & \mathbf{0} & \mathbf{0}
\end{bmatrix}
\begin{bmatrix}
\boldsymbol{T}_{0} \\ \mathbf{0} \\ \boldsymbol{T}_{1} \\ \mathbf{0} \\ \mathbf{0} \\ \boldsymbol{T}_{5} \\ \mathbf{0} \\ \mathbf{0} \\ \mathbf{0}
\end{bmatrix}
\tag{40}
$$

where,

$$
\boldsymbol{A}^{B\pm} = \begin{bmatrix} \boldsymbol{A}_{0}^{B\pm} \\ \boldsymbol{A}_{3-}^{B\pm} \\ \boldsymbol{A}_{1}^{B\pm} \\ \boldsymbol{A}_{3+}^{B\pm} \end{bmatrix} \quad \boldsymbol{A}^{A\pm} = \begin{bmatrix} \boldsymbol{A}_{3-}^{A\pm} \\ \boldsymbol{A}_{5}^{A\pm} \\ \boldsymbol{A}_{3+}^{A\pm} \end{bmatrix} \tag{41}
$$

5. Numerical results

In this section, some numerical examples are illustrated to show the validity and effectiveness of this modified BEM for 2-D Love-wave model. In the following numerical examples, the material parameters of the layer and half-plane are dimensionless, which have a shear modulus ratio of $\mu^B / \mu^A = 1.8$, a longitudinal wave velocity ratio of $c_T^B / c_T^A = 0.78$, and the dimensionless frequency is taken as $\bar{\omega} = 2\omega H / \left(c_T^A \pi\right)$. The element size is selected to have at least 32 elements per Love wavelength λ_L , which provides accurate results for 2-D elasto-dynamic problem.

Firstly, the numerical results obtained by the modified BEM will be compared with theoretical far-field Green's functions. As shown in Fig.4, this numerical model is a 2-D semi-finite space with unit harmonic line source acting in x_3 direction, with the distance d between source and lower interface of the upper layer. The far-field amplitudes are presented in Tab.1 for various frequencies $\bar{\omega}$ =1.2, 6.5, 10.8, while a fixed height d =0.5*H*. The far-field coefficients of Love waves are obtained by modified BEM and compared with theoretical results**Error! Reference source not found.**]**Error! Reference source not found.**]. The results are in excellent agreement (see Tab.1), which show the validity of this modified BEM for a certain range of frequencies. From additional parametric study, it is found from Fig.5 that, as the source are moved closer to the top surface, e.g. $d = 0.1\text{-}0.9H$, longer surface lengths should be remained in the BEM model to ensure the accuracy, which should be kept in mind as a criterion for accurate calculations of these numerical results.

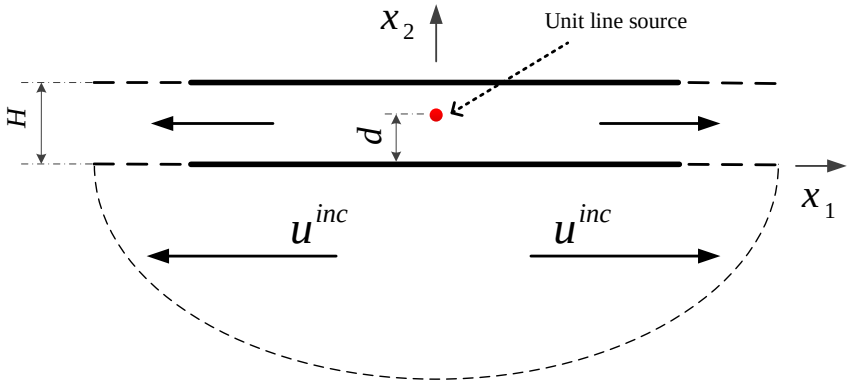

Fig. 4. Schematic diagram for the unit line source problem.

Table 1. Comparisons with truncated locations at $\bar{x} = \pm 60\lambda_L / H$ (λ_L being the Love wavelength for the lowest mode) for the unit line source problem.

Frequency $\bar{\omega}$	Modal	BEM results (Far-field amplitudes)	theoretical far-field Green's functions
1.2	Modal 1	0.13562i	0.13557i
6.5	Modal 1	0.01634i	0.01635i
	Modal 2	0.01335i	0.01335i
10.8	Modal 1	0.00709i	0.00705i
	Modal 2	0.00983i	0.00983i
	Modal 3	-0.0358i	-0.0358i

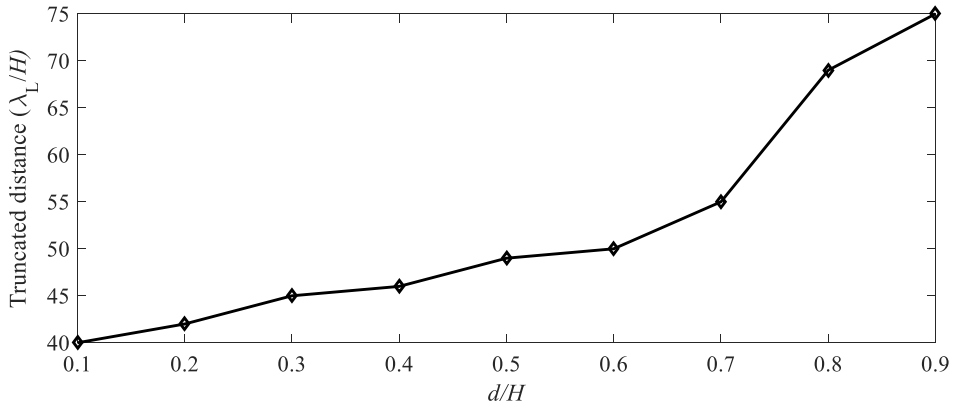

Fig. 5. Proper truncation distance with various d for the unit line source problem.

Next, the lowest incident Love-wave mode for a fixed frequency is selected to impinge onto a cavity defect of arc surface on the bonding interface, with radius $R_1 = H$ and height h (see Fig.6). The transmission and reflection coefficients for each modal at various frequencies: $\bar{\omega}$ =0.8, 5, 9.5, are shown in Tab.2. And the normalized displacements for the same frequency range which are here defined as $U^{\pm}_{scat} / \sum_{i=1}^{n} R_i^{\pm} r_i^{\pm}$ are plotted. It is observed from Fig.7(a)-7(c) that the scattered displacements are approximated by Love surface waves at far ends, which satisfy the assumptions of Eq.(6).

For basic check purposes, propagations in the opposite directions for the same frequency range are considered, and numerical solutions show very good agreement in all cases owing to the symmetry of the defect. Furthermore, a parametric study has been carried out to analyze the influence of defect height h =0.2, 0.4, 0.6, 0.8, on the reflected and transmitted amplitudes which are defined as $A^{ref} = u^{-}_{scat} / u^{-}$ and $A^{trans} = \left(u^{+}_{scat} + u^{inc}\right) / u^{+}$. It is found from Fig.8 that as the defect becomes larger, the absolute value of the transmitted amplitude gradually decreases and the absolute value of the reflected amplitude is diverse.

Table 2. The transmission and reflection coefficients with truncated locations at $\bar{x} = \pm 60\lambda_L / H$, h=0.2, (λ_L being the Love wavelength for the lowest mode) for a circle arc defect at the bonding interface.

Frequency $\bar{\omega}$	Modal	Reflection coefficients	Transmission coefficients
0.8	Modal 1	0.00039-0.07060i	-0.00582+0.03457i
5	Modal 1	-0.04383+0.10690i	0.01638+0.02342i
	Modal 2	-0.11344+0.06911i	0.07724+0.11906i
9.5	Modal 1	-0.03315+0.08802i	0.00531+0.00383i
	Modal 2	-0.19330+0.36373i	0.04204+0.03600i
	Modal 3	-0.22045-0.05598i	0.07071+0.09606i

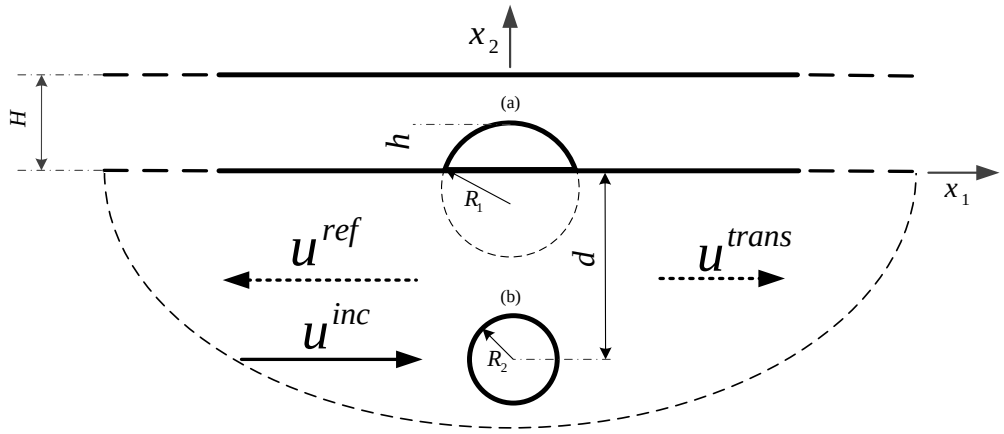

Fig. 6. Schematic diagram for Love-wave scattering problem: (a) a cavity defect of arc surface on the bonding interface, with radius R_1, height h; (b)a circle defect in half-plane with radius R_2, depth d.

Finally, we consider the lowest incident Love-wave mode for a fixed frequency impinging onto the circle defect in half-plane with radius $R_2 = 0.2H$ and depth $d = 0.5H$, in the positive direction of x_1 (see Fig.6(b)). The transmission and reflection coefficients of various frequencies: $\bar{\omega}$ =0.8, 5, 9.5, are performed in Table 3. As the relative normalized displacements are plotted in Fig. 9(a)-9(c). we could get the same conclusion that the scattered displacements are approximated by Love surface waves at far ends. Also, numerical results for propagation in opposite direction show very good agreement due to the symmetry of the defect.

Table 3. The transmission and reflection coefficients with truncated locations at $\bar{x} = \pm 60\lambda_L / H$, R_2=0.2, d=0.5 (λ_L being the Love wavelength for the lowest mode) for a circle defect in half-plane.

Frequency $\bar{\omega}$	Modal	Reflection coefficients	Transmission coefficients
0.8	Modal 1	-0.00026+0.00746i	-0.00026+0.00758i
5	Modal 1	-0.00004+0.00052i	-0.00028+0.00202i
	Modal 2	0.00046+0.00494i	-0.00190+0.01682i
9.5	Modal 1	0.00001-0.00001i	-0.00002+0.00010i
	Modal 2	0.00003-0.00005i	-0.00017+0.00090i
	Modal 3	0.00018-0.00027i	-0.00060+0.00375i

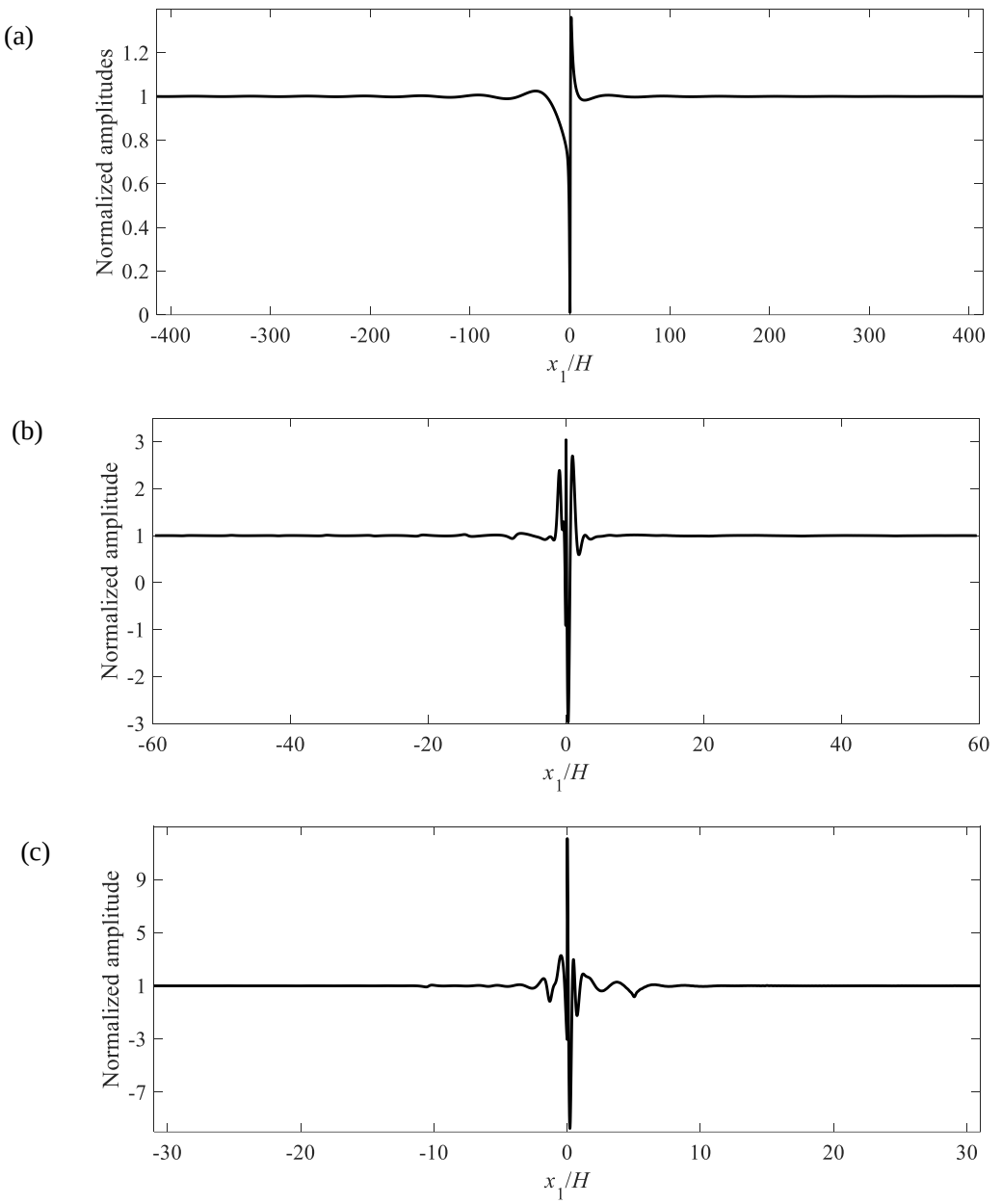

Fig. 7. Normalized amplitudes of upper boundary due to a defect at the bonding interface: (a) $\bar{\omega}=0.8$; (b) $\bar{\omega}=5$; (c) $\bar{\omega}=9.5$.

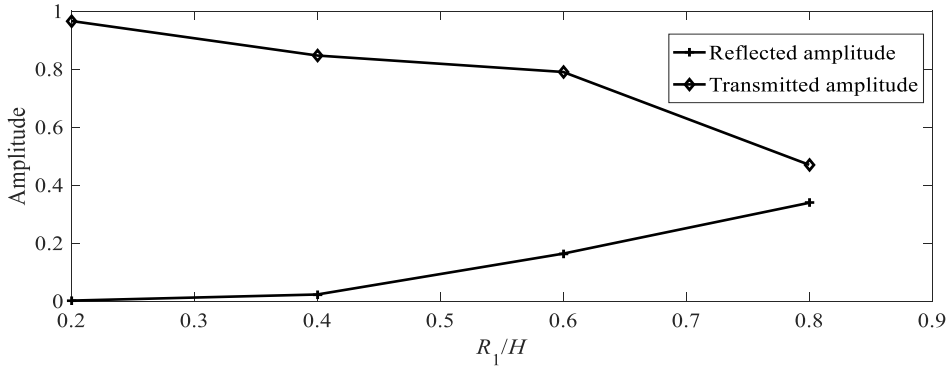

Fig. 8. Reflected and transmitted amplitudes due to a defect at the bonding interface.

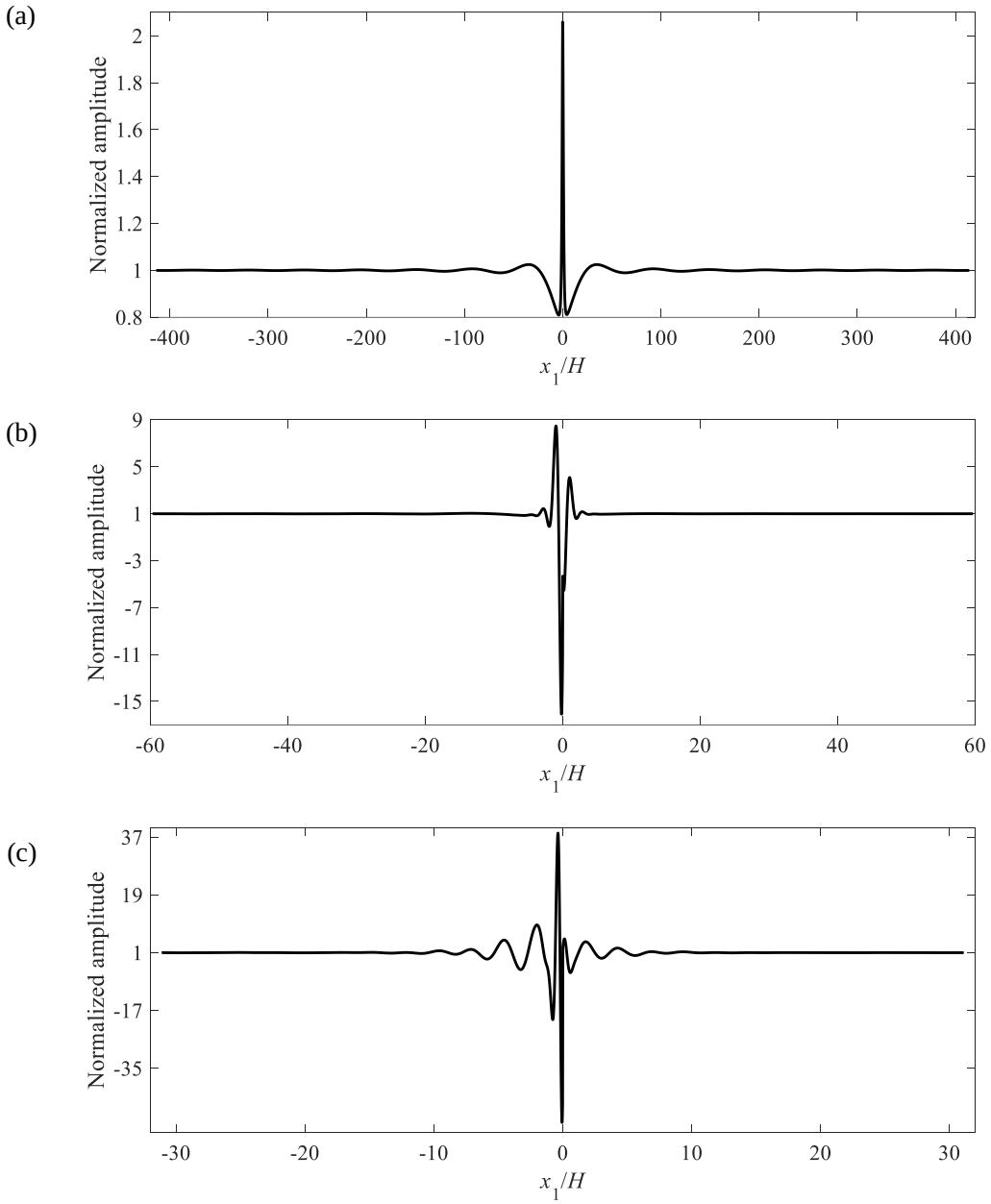

Fig. 9. Normalized amplitudes of upper boundary due to a circle defect in half-plane: (a) $\bar{\omega} = 0.8$; (b) $\bar{\omega} = 5$; (c) $\bar{\omega} = 9.5$ **.**

6. Conclusion

In this paper, we proposed a modified BEM for scattering problem of Love surface wave by a defect at the bonding interface. The guided Love-wave displacement patterns are assumed on the far-field infinite boundaries previously omitted, and they are incorporated into the BEM system as the modified items. With this improvement, the spurious reflected waves were eliminated. The validity and effectiveness of this modified BEM were numerically checked by theoretical far-field Green's functions. Various parametric results show that this method can be applied on the Love-wave model with a defect of arbitrary shape and location, and as the geometrical size of the defect becomes larger, the transmitted wave gradually decreases and the reflected wave is diverse.

In the future, the scattering data from forward analysis by this modified BEM, will be used for the inverse analysis of reconstructing both the location and specific geometric information of the debonding cavities.

Conflicts of Interest

The authors declare that they have no conflicts of interest.

Acknowledgements

This work was supported by the National Natural Science Foundation of China (Nos. 11502108, 11611530686, 11232007), the Natural Science Foundation of Jiangsu Province (No. BK20140037), and a project Funded by the Priority Academic Program Development of Jiangsu Higher Education Institutions (PAPD).

References

[1] J.L. Rose, "A baseline and vision of ultrasonic guided wave inspection potential," *J. Press. Vess. T. ASME*, vol. 124, no. 3, pp. 273–282, 2002.
[2] A.C. Raghavan, C.E.S. Cesnik, "Review of guided-wave structural health monitoring," *Shock Vib. Digest*, vol. 39, no. 2, pp. 91–114, 2007.
[3] M. Capriotti, H.E. Kim, F.L.D. Scalea et al., "Non-destructive inspection of impact damage in composite aircraft panels by ultrasonic guided waves and statistical processing," *Materials*, vol. 10, no. 6, pp. 616, 2017.
[4] K.M. Qatu, A. Abdelgawad, K. Yelamarthi, "Structure damage localization using a reliable wave damage detection technique," *2016 International conference on electrical, electronics, and optimization techniques*, pp. 1959–1962, 2016.
[5] W. Wang, H. Zhang, J.P. Lynch et al., "Numerical and experimental simulation of linear shear piezoelectric phased arrays for structural health monitoring," *Nondestructive characterization and monitoring of advanced materials, aerospace, civil infrastructure*, vol. 10169, Article ID 1016912, 2017.
[6] E.V. Malyarenko, M.K. Hinders, "Ultrasonic Lamb wave diffraction tomography," *Ultrasonics*, vol. 39, no. 4, pp. 269–281, 2001.
[7] B. Wang, S. Hirose, "Inverse problem for shape reconstruction of plate-thinning by guided SH-waves," *Meta. Trans*, vol. 53, no. 10, pp. 1782-1789, 2012.
[8] B. Wang, S. Hirose, "Shape reconstruction of plate thinning using reflection coefficients of ultrasonic Lamb waves: a numerical approach," *ISIJ Int.*, vol. 52, no. 7, pp. 1320-1327, 2012.
[9] B. Wang, Y. Da, Z. Qian, "Reconstruction of surface flaw shape using reflection data of guided Rayleigh surface waves," *Int. J. Appl. Electrom.*, vol. 52, no. 1-2, pp. 41-48, 2016.
[10] R Kakar, "Love waves in Voigt-type viscoelastic inhomogeneous layer overlying a gravitational half-space," *Int. J. Geomech.*, vol. 16, no. 3, Article ID 04015068, 2016.
[11] P. Destuynder, C. Fabre, "Few remarks on the use of Love waves in non-destructive testing," *Discrete Cont. Dyn. S*, vol. 9, no. 2, pp. 427-444, 2016.
[12] X. Jiang, P. Li, J. Lyu et al., "An adaptive finite element method for the wave scattering with transparent boundary condition," *J. Sci. Comput.*, vol. 72, no. 3, pp. 936-956, 2017.
[13] J.D. Achenbach, "Acoustic emission from a surface-breaking crack in a layer under cyclic loading," *J. Mech. Mata. Struct.*, vol. 4, no. 4, pp. 649-657, 2009.
[14] A. Gunawan, S. Hirose, "Mode-exciting method for Lamb wave-scattering analysis," *J. Acoust. Soc. Am.*, vol. 115, no. 3, pp. 996-1005, 2004.
[15] P.C. Waterman, "Matrix theory of elastic wave scattering," *J. Acoust. Soc. Am.*, vol. 60, no. 3, pp. 567-80, 1976.
[16] I. Herrera, "On a method to obtain a Green's function for a multi-layered half-space," *B. Seismol. Soc. Am.*, vol. 54, no. 4, pp. 1087-1096, 1964.
[17] J. D. Achenbach, Reciprocity in Elastiodynamics, Cambridge University Press, Cambridge, UK, 2003.
[1] D.E. Beskos, U. Heise, Boundary Element Methods in Mechanics, North-Holland, Amsterdam, the Netherlands, 1987.